Granular Matter (2012) 14:607–619
DOI 10.1007/s10035-012-0360-1

ORIGINAL PAPER

Granular contact dynamics with particle elasticity

K. Krabbenhoft · J. Huang · M. Vicente da Silva · A. V. Lyamin

Received: 22 November 2011 / Published online: 26 July 2012

Abstract A granular contact dynamics formulation for elastically deformable particles is detailed. The resulting scheme bears some similarity to traditional molecular dynamics schemes in that the consideration of a finite elastic contact stiffness implies the possibility for inter-particle penetration. However, in contrast to traditional molecular dynamics schemes, there are no algorithmic repercussions from operating with a large or, in the extreme case infinite, contact stiffness. Indeed, the algorithm used—a standard second-order cone programming solver—is independent of the particle scale model and is applicable to rigid as well as elastically deformable particles.

Keywords Contact dynamics · Discrete element method · DEM · Elasticity

1 Introduction

The motion and interaction of discrete particles can be simulated using one of two different methods. The most popular method is the discrete (or distinct) element method (DEM) pioneered by Cundall [1]. In this method, which is often referred to as a molecular dynamics (MD) method, the positions of the particles are advanced in a fully explicit manner using sufficiently small time steps. Interaction between grains is accounted for by relating the overlap that may occur between particles to forces via an appropriate constitutive relation. While the motivation for this approach to some extent is algorithmic, the penetration that occurs at particle contacts may be interpreted as the actual deformation associated with particles of finite rigidity [2] and the microscopic elastic constants (normal and tangential spring stiffnesses) can be related to the equivalent macroscopic quantities (bulk and shear modulus) [3–5]. However, in many cases involving the flow and deformation of granular materials, the macroscopic system stiffness is orders of magnitude lower than the microscopic inter-particle stiffness. As such, the inter-particle stiffness is often chosen as a compromise between the physics (large enough to not affect the response significantly) and the computational performance (small enough to not require a prohibitively small time step). A typical example of such a compromise is described in [6].

The second approach to the modeling of granular assemblies is the so-called non-smooth contact dynamics (CD) method originally developed by Moreau et al. [7–10]. In the most basic version of this method, the particles are considered perfectly rigid and the contact forces are determined as those that exactly prevent inter-particle penetration. An implicit time discretization is usually employed, thus allowing for larger time steps, and implying that collisions are 'smeared' over a finite time interval. A key point often stressed in connection with the CD method is that assemblies consisting of perfectly rigid particles do not allow for the propagation of waves at a finite speed. However, in many scenarios of practical interest, wave propagation is of little significance, as is elastic particle deformation, and the two methods then lead to practically identical results (subject to identical tolerances

K. Krabbenhoft (✉) · J. Huang · M. V. da Silva · A. V. Lyamin
Centre for Geotechnical Science and Engineering,
University of Newcastle, Callaghan, NSW, Australia
e-mail: kristian.krabbenhoft@gmail.com;
kristian.krabbenhoft@newcastle.edu.au

K. Krabbenhoft
Institute of Technology and Innovation,
University of Southern Denmark, Odense, Denmark

M. V. da Silva
Department of Civil Engineering, Faculty of Sciences and Technology,
Universidade Nova de Lisboa, Lisbon, Portugal

being specified). Examples of application of the CD method to the simulation of granular materials include [11–29].

Though aimed at simulating essentially the same physics, the basic premises and the algorithmic implementations of the MD and CD methods are so different that they are often considered two distinct methods, each with a set of inherent assumptions that cannot be easily circumvented. In particular, while the concept of particle deformability is at the heart of the MD method, it is sometimes held that the assumption of perfectly rigid particles is fundamental to the CD method. However, as discussed by a number of authors, notably [30,31], the CD method is in fact quite general and in principe capable of accommodating any particle scale behaviour. In this paper, the case of elastically deformable particles is considered in detail. As in MD, the assumption of a finite elastic contact stiffness leads to a situation where particles may penetrate each other. In contrast to MD, however, the consideration of particle deformability is motivated solely by the physics rather than the numerics. Moreover, the basic CD framework is maintained and algorithms originally developed for the perfectly rigid case are applicable with little modification. In the present paper, we demonstrate this fact with respect to an optimization based solution scheme previously developed for the perfectly rigid case [32].

The paper is organized as follows. In Sect. 2, the governing equations for frictionless rigid particles are summarized. In the interest of clarity, the methodology is developed with respect to two-dimensional circular particles. However, the basic principles are straightforward to generalize to three dimensions. One possible extension is outlined in "Appendix 1". Following [32] we make extensive use of variational concepts. This sets the scene for subsequent developments. In Sect. 3 the framework is extended to elastically deformable particles and in Sect. 4 inter-particle friction is included. Finally, in Sect. 5, the effects of a finite elastic inter-particle stiffness are illustrated with respect to the common biaxial test before conclusions are drawn in Sect. 6.

2 Frictionless rigid particles

2.1 Equations of motion

The equations of motion for a single frictionless rigid particle are given by

$$m\dot{\boldsymbol{v}}(t) = \boldsymbol{f}_{\text{ext}} \tag{1}$$

where $\boldsymbol{v}(t) = (v_x(t), v_y(t))^{\mathsf{T}}$ are the linear velocities, m is the mass, and $\boldsymbol{f}_{\text{ext}} = (f_x, f_y)^{\mathsf{T}}_{\text{ext}}$ are external forces.

2.1.1 Time discretization

Relating position to velocity by $\dot{\boldsymbol{x}}(t) = \boldsymbol{v}(t)$, the equations of motion can be written as

$$\begin{aligned} m\dot{\boldsymbol{v}}(t) &= \boldsymbol{f}_{\text{ext}} \\ \boldsymbol{v}(t) &= \dot{\boldsymbol{x}}(t) \end{aligned} \tag{2}$$

These equations are discretized in time by the θ-method:

$$\begin{aligned} m\frac{\boldsymbol{v}-\boldsymbol{v}_0}{\Delta t} &= \boldsymbol{f}_{\text{ext}} \\ \theta\boldsymbol{v} + (1-\theta)\boldsymbol{v}_0 &= \frac{\boldsymbol{x}-\boldsymbol{x}_0}{\Delta t} \end{aligned} \tag{3}$$

where $0 \leq \theta \leq 1$ and $\boldsymbol{x}_0$ and $\boldsymbol{v}_0$ are the known position and velocity at time t_0 while $\boldsymbol{x}$ and $\boldsymbol{v}$ are the corresponding quantities at time $t_0 + \Delta t$. We have here assumed that $\boldsymbol{f}_{\text{ext}}$ are constant, stemming, for example, from gravity. Straightforward manipulations lead to the following expressions for the displacements and velocities at time $t_0 + \Delta t$:

$$\begin{aligned} \bar{m}\Delta\boldsymbol{x} &= \bar{\boldsymbol{f}}_0 \\ \boldsymbol{v} &= \frac{1}{\theta}\left[\frac{\Delta\boldsymbol{x}}{\Delta t} - (1-\theta)\boldsymbol{v}_0\right] \end{aligned} \tag{4}$$

where

$$\bar{m} = \frac{1}{\theta\Delta t^2}m, \quad \bar{\boldsymbol{f}}_0 = \boldsymbol{f}_{\text{ext}} + \bar{m}\boldsymbol{v}_0\Delta t \tag{5}$$

and $\Delta\boldsymbol{x} = \boldsymbol{x} - \boldsymbol{x}_0$ are the displacements. The stability properties of the θ-method are well known [33]: for $\theta = \frac{1}{2}$ the an unconditionally stable and energy preserving scheme is recovered, for $\theta > \frac{1}{2}$ the scheme is unconditionally stable and dissipative, and for $\theta < \frac{1}{2}$ stability depends on the time step. In the context of collisions, the algorithmic energy dissipation that occurs for $\theta > \frac{1}{2}$ can be related to the physical dissipation associated with impact and thus to the restitution coefficient. Indeed, as shown in [32], a value of $\theta = \frac{1}{2}$ corresponds to an elastic collision while $\theta = 1$ reproduces a perfectly inelastic collision.

2.2 Non-penetration condition

Consider two circular particles as shown in Fig. 1. The positions of the particles at time t_0 are given by $\boldsymbol{x}_0^i$ and $\boldsymbol{x}_0^j$. The condition that the particles do not penetrate each other at time $t_0 + \Delta t$ can be stated as

$$||\boldsymbol{x}^i - \boldsymbol{x}^j|| \geq r^i + r^j \tag{6}$$

This inequality constraint is non-convex for spatial dimensions greater than one and thus problematic to deal with. Consequently, throughout this paper, we consider the linear approximation:

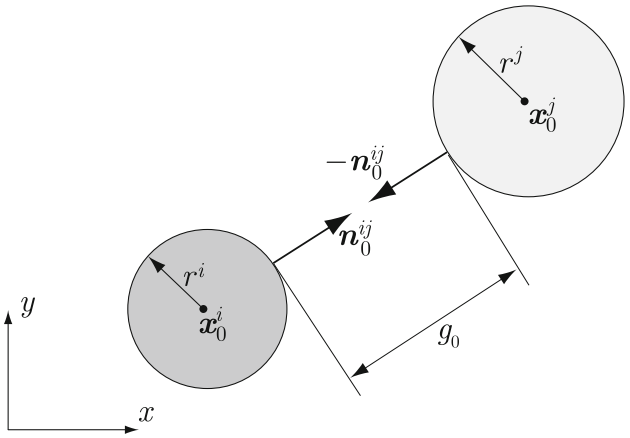

Fig. 1 Frictionless contact geometry

$$\left(\boldsymbol{n}_0^{ij}\right)^{\mathsf{T}}(\Delta\boldsymbol{x}^i - \Delta\boldsymbol{x}^j) \le g_0 \tag{7}$$

where

$$\boldsymbol{n}_0^{ij} = \frac{\boldsymbol{x}_0^j - \boldsymbol{x}_0^i}{||\boldsymbol{x}_0^i - \boldsymbol{x}_0^j||}, \quad g_0 = ||\boldsymbol{x}_0^i - \boldsymbol{x}_0^j|| - (r^i + r^j) \tag{8}$$

are the initial normal and gap respectively (see Fig. 1). The linearized non-penetration can also be derived by expanding the exact expression (6) in time and then using the θ-method with $\theta = 0$ to express the velocities in terms of the displacements. As such, the linearized non-penetration condition may be viewed as being imposed in a fully explicit manner. In other words, it is assumed that the geometry does not change over the time step. Although this could potentially compromise the stability of the system, practical experience shows that stability for all but obviously unreasonable time steps always is maintained.

2.3 Governing equations

We now consider the problem of frictionless contact involving two particles, i and j. In this case the governing equations comprise momentum balance for each particle (incorporating contact forces), the linearized non-penetration condition and conditions ensuring that the contact forces are positive only if the gap is closed and otherwise zero. These requirements can be stated in terms of the following time discrete governing equations:

$$\begin{aligned}
&\bar{m}^i\Delta\boldsymbol{x}^i = \bar{\boldsymbol{f}}_0^i - \boldsymbol{n}_0^{ij}\,p\\
&\bar{m}^j\Delta\boldsymbol{x}^j = \bar{\boldsymbol{f}}_0^j + \boldsymbol{n}_0^{ij}\,p\\
&\left(\boldsymbol{n}_0^{ij}\right)^{\mathsf{T}}(\Delta\boldsymbol{x}^i - \Delta\boldsymbol{x}^j) \le g_0\\
&p \ge 0\\
&p\left[\left(\boldsymbol{n}_0^{ij}\right)^{\mathsf{T}}(\Delta\boldsymbol{x}^i - \Delta\boldsymbol{x}^j) - g_0\right] = 0
\end{aligned} \tag{9}$$

where p is the contact force. The above governing equations may be viewed as the optimality conditions associated with one of four different optimization problems, or variational principles. This is discussed in detail in the following sections

2.4 Variational formulation

Before proceeding with a variational formulation of the governing equations (9), it is convenient to introduce the following matrix quantities which cover general n-particle systems:

$$\begin{aligned}
&\bar{\boldsymbol{M}} = \mathrm{diag}(\bar{m}^1, \bar{m}^1, \ldots, \bar{m}^n, \bar{m}^n)\\
&\boldsymbol{x} = (\boldsymbol{x}^1, \ldots, \boldsymbol{x}^n), \quad \boldsymbol{v} = (\boldsymbol{v}^1, \ldots, \boldsymbol{v}^n)\\
&\boldsymbol{g} = (g^1, \ldots, g^N), \quad \boldsymbol{p} = (p^1, \ldots, p^N)
\end{aligned} \tag{10}$$

where n is the number of particles and N is the number of contacts. Furthermore, collecting the normals associated with potential contacts in a matrix $\boldsymbol{N}$, the governing equations (9) can be written as

$$\begin{aligned}
&\bar{\boldsymbol{M}}\Delta\boldsymbol{x} + \boldsymbol{N}_0\boldsymbol{p} = \bar{\boldsymbol{f}}_0\\
&\boldsymbol{N}_0^{\mathsf{T}}\Delta\boldsymbol{x} \le \boldsymbol{g}_0\\
&\boldsymbol{p} \ge \boldsymbol{0}\\
&\boldsymbol{P}\left(\boldsymbol{N}_0^{\mathsf{T}}\Delta\boldsymbol{x} - \boldsymbol{g}_0\right) = \boldsymbol{0}
\end{aligned} \tag{11}$$

where $\boldsymbol{P} = \mathrm{diag}(\boldsymbol{p})$ and subscripts 0 again refer to the known state. These equations constitute the first-order Karush–Kuhn–Tucker (KKT) optimality conditions associated with the following optimization problem (see "Appendix 3" for details):

$$\begin{aligned}
\min_{\Delta\boldsymbol{x}}\max_{\boldsymbol{p}} \quad & \left\{\tfrac{1}{2}\Delta\boldsymbol{x}^{\mathsf{T}}\bar{\boldsymbol{M}}\Delta\boldsymbol{x} - \Delta\boldsymbol{x}^{\mathsf{T}}\bar{\boldsymbol{f}}_0\right\}\\
& + \left\{\Delta\boldsymbol{x}^{\mathsf{T}}\boldsymbol{N}_0\boldsymbol{p} - \boldsymbol{g}_0^{\mathsf{T}}\boldsymbol{p}\right\}\\
\text{subject to} \quad & \boldsymbol{p} \ge \boldsymbol{0}
\end{aligned} \tag{12}$$

The first term in the objective function is a time discrete form of the action integral associated with a collection of non-interacting particles while the second term accounts for the effects of contact. This principle reproduces the governing equations (11) after which the velocities at time $t = t_1 = t_0 + \Delta t$ are calculated from the second equation of (4) and used to set up a new optimization problem to determine the displacements at time t_2, etc.

Alternatively, the governing equations are recovered as the solution to the following problem:

$$\begin{aligned}
\min_{\Delta\boldsymbol{x}}\max_{\boldsymbol{t},\boldsymbol{p}} \quad & -\left\{\tfrac{1}{2}\boldsymbol{t}^{\mathsf{T}}\bar{\boldsymbol{M}}^{-1}\boldsymbol{t} - \Delta\boldsymbol{x}^{\mathsf{T}}(\boldsymbol{t} - \bar{\boldsymbol{f}}_0)\right\}\\
& + \left\{\Delta\boldsymbol{x}^{\mathsf{T}}\boldsymbol{N}_0\boldsymbol{p} - \boldsymbol{g}_0^{\mathsf{T}}\boldsymbol{p}\right\}\\
\text{subject to} \quad & \boldsymbol{p} \ge \boldsymbol{0}
\end{aligned} \tag{13}$$

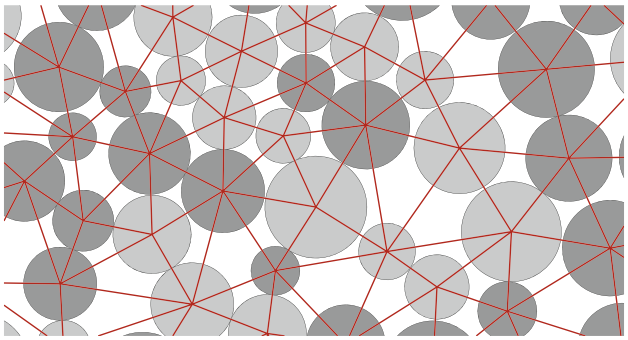

Fig. 2 Potential contacts as given by Delaunay triangulation

where $\boldsymbol{t}$ are to be interpreted as dynamics forces (one of the optimality conditions associated with the above problem gives the relation $\boldsymbol{t} = \bar{\boldsymbol{M}}\Delta\boldsymbol{x}$).

2.4.1 Displacement based problem

Solving the max part of the problem (12) gives rise to the following displacement based problem:

$$\begin{aligned} &\text{minimize} && \tfrac{1}{2}\Delta\boldsymbol{x}^{\mathsf{T}}\bar{\boldsymbol{M}}\Delta\boldsymbol{x} - \Delta\boldsymbol{x}^{\mathsf{T}}\bar{\boldsymbol{f}}_0 \\ &\text{subject to} && \boldsymbol{N}_0^{\mathsf{T}}\Delta\boldsymbol{x} - \boldsymbol{g}_0 \le \boldsymbol{0} \end{aligned} \tag{14}$$

The contact forces are here recovered as part of the solution, namely as the Lagrange multipliers associated with the inequality constraints.

2.4.2 Force based problem

Similarly, solving the min part of (13) gives rise to the following force based problem:

$$\begin{aligned} &\text{maximize} && -\tfrac{1}{2}\boldsymbol{t}^{\mathsf{T}}\bar{\boldsymbol{M}}^{-1}\boldsymbol{t} - \boldsymbol{g}_0^{\mathsf{T}}\boldsymbol{p} \\ &\text{subject to} && \boldsymbol{t} + \boldsymbol{N}_0\boldsymbol{p} = \bar{\boldsymbol{f}}_0 \\ & && \boldsymbol{p} \ge \boldsymbol{0} \end{aligned} \tag{15}$$

The displacements are here recovered as the Lagrange multipliers associated with the equality constraints.

In summary, the governing equations (11) can be cast in terms of four different but equivalent variational statements: the mixed force-displacement problems (12) and (13), the displacement based problem (14), and the force based problem (15). Each of these four problems have their merits in terms of providing physical insights and forming the basis for computations.

2.5 Potential contact specification

Following [32], potential contacts at $t_0 + \Delta t$ are defined by a Delaunay triangulation on the basis of the positions at t_0. An example is shown in Fig. 2.

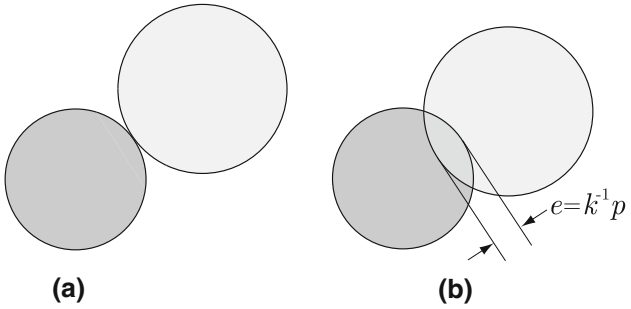

Fig. 3 Contact between perfectly rigid (**a**) and elastic (**b**) particles

3 Frictionless elastic particles

The above model is now extended to cover elastically deformable particles. Adopting an approach equivalent to that of MD where the elastic contact forces are proportional to the inter-particle penetration, the only modification required concerns the measure of the gap g_0. Thus, instead of requiring the non-penetration condition satisfied exactly, we allow for a penetration equal to $k^{-1}p$ where k is a constant characterizing the effective stiffness of the contact (see Fig. 3). The governing equations (9) for a binary system are thus given by

$$\begin{aligned} &\bar{m}^i\Delta\boldsymbol{x}^i = \bar{\boldsymbol{f}}_0^i - \boldsymbol{n}_0^{ij}p \\ &\bar{m}^j\Delta\boldsymbol{x}^j = \bar{\boldsymbol{f}}_0^j + \boldsymbol{n}_0^{ij}p \\ &\left(\boldsymbol{n}_0^{ij}\right)^{\mathsf{T}}(\Delta\boldsymbol{x}^i - \Delta\boldsymbol{x}^j) \le g_0 + k^{-1}p \\ &p \ge 0 \\ &p\left[\left(\boldsymbol{n}_0^{ij}\right)^{\mathsf{T}}(\Delta\boldsymbol{x}^i - \Delta\boldsymbol{x}^j) - g_0 - k^{-1}p\right] = 0 \end{aligned} \tag{16}$$

while, for a n-particle system, (11) generalizes to

$$\begin{aligned} &\bar{\boldsymbol{M}}\Delta\boldsymbol{x} + \boldsymbol{N}_0\boldsymbol{p} = \bar{\boldsymbol{f}}_0 \\ &\boldsymbol{N}_0^{\mathsf{T}}\Delta\boldsymbol{x} \le \boldsymbol{g}_0 + \boldsymbol{C}\boldsymbol{p} \\ &\boldsymbol{p} \ge \boldsymbol{0} \\ &\boldsymbol{P}(\boldsymbol{N}_0^{\mathsf{T}}\Delta\boldsymbol{x} - \boldsymbol{g}_0 - \boldsymbol{C}\boldsymbol{p}) = \boldsymbol{0} \end{aligned} \tag{17}$$

where $\boldsymbol{C} = \operatorname{diag}(1/k^1, \ldots, 1/k^N)$ contains the contact spring compliances.

3.1 Variational formulation

The governing equations (17) may again be thought of as constituting the optimality conditions associated with a number of different optimization problems. One possibility is to

extend min-max problem (13) to account for a finite particle stiffness. This gives rise to the following problem:

$$\begin{aligned}\min_{\Delta x}\max_{p,t}\ & -\left\{\tfrac{1}{2}\boldsymbol{t}^{\mathsf{T}}\bar{\boldsymbol{M}}^{-1}\boldsymbol{t}-\Delta\boldsymbol{x}^{\mathsf{T}}(\boldsymbol{t}-\bar{\boldsymbol{f}}_0)\right\}\\ & +\left\{\Delta\boldsymbol{x}^{\mathsf{T}}\boldsymbol{N}_0\boldsymbol{p}-\boldsymbol{g}_0^{\mathsf{T}}\boldsymbol{p}-\tfrac{1}{2}\boldsymbol{p}^{\mathsf{T}}\boldsymbol{C}\,\boldsymbol{p}\right\}\\ \text{subject to}\quad & \boldsymbol{p}\geq\boldsymbol{0}\end{aligned}\tag{18}$$

We note the similarity of this problem to the classical Hellinger–Reissner variational principle [34–37]. Similarly, the extension of (12) to account for particle elasticity can be carried out in two ways: either by introducing the elastic energy term $\frac{1}{2}\boldsymbol{p}^{\mathsf{T}}\boldsymbol{C}\,\boldsymbol{p}$ as above or by introducing the elastic energy in terms of additional kinematic variables (see "Appendix 3" for details).

3.1.1 Force based problem

The force based version of (18) follows by solving its min part to arrive at

$$\begin{aligned}\text{maximize}\quad & -\tfrac{1}{2}\boldsymbol{t}^{\mathsf{T}}\bar{\boldsymbol{M}}^{-1}\boldsymbol{t}-\boldsymbol{g}_0^{\mathsf{T}}\boldsymbol{p}-\tfrac{1}{2}\boldsymbol{p}^{\mathsf{T}}\boldsymbol{C}\,\boldsymbol{p}\\ \text{subject to}\quad & \boldsymbol{t}+\boldsymbol{N}_0\boldsymbol{p}=\bar{\boldsymbol{f}}_0\\ & \boldsymbol{p}\geq\boldsymbol{0}\end{aligned}\tag{19}$$

where the only modification with respect to (15) is the addition of the quadratic term accounting for particle elasticity to the objective function.

4 Frictional elastic particles

The most general case of frictional elastic particles is considered next. Following [32] this problem appears by adding appropriate tangential forces and accounting for the moments induced by these tangential forces. The frictionless problem (19) thus generalizes to

$$\begin{aligned}\min_{\Delta x,\Delta\alpha}\max_{p,q,t,r}\ & -\left\{\tfrac{1}{2}\boldsymbol{t}^{\mathsf{T}}\bar{\boldsymbol{M}}^{-1}\boldsymbol{t}-\Delta\boldsymbol{x}^{\mathsf{T}}(\boldsymbol{t}-\bar{\boldsymbol{f}}_0)\right\}\\ & +\left\{\Delta\boldsymbol{x}^{\mathsf{T}}\boldsymbol{N}_0\boldsymbol{p}-\boldsymbol{g}_0^{\mathsf{T}}\boldsymbol{p}-\tfrac{1}{2}\boldsymbol{p}^{\mathsf{T}}\boldsymbol{C}_N\boldsymbol{p}\right\}\\ & -\left\{\tfrac{1}{2}\boldsymbol{r}^{\mathsf{T}}\bar{\boldsymbol{J}}^{-1}\boldsymbol{r}-\Delta\boldsymbol{\alpha}^{\mathsf{T}}(\boldsymbol{r}-\bar{\boldsymbol{m}}_0)\right\}\\ & +\left\{\Delta\boldsymbol{x}^{\mathsf{T}}\hat{\boldsymbol{N}}_0\boldsymbol{q}-\Delta\boldsymbol{\alpha}^{\mathsf{T}}\boldsymbol{R}_0\boldsymbol{q}-\tfrac{1}{2}\Delta\boldsymbol{q}^{\mathsf{T}}\boldsymbol{C}_T\Delta\boldsymbol{q}\right\}\\ \text{subject to}\quad & |\boldsymbol{q}|-\mu\boldsymbol{p}\leq\boldsymbol{0}\end{aligned}\tag{20}$$

where the third and fourth terms in the objective function account for sliding and rolling due to tangential forces. The tangential forces, aligned along $\hat{\boldsymbol{n}}_0^{ij}$ (see Fig. 4), are given by $\boldsymbol{q}$, while the angles of rotation are given by $\boldsymbol{\alpha}$. Elastic deformations are now accounted for by two contributions: one concerning normal deformations governed by effective contact compliances $\boldsymbol{C}_N=\mathrm{diag}(1/k_N^1,\ldots,1/k_N^N)$

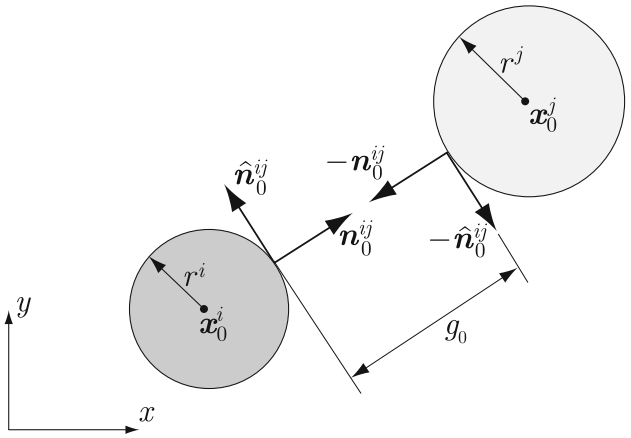

Fig. 4 Frictional contact geometry

and one concerning tangential deformations governed by $\boldsymbol{C}_T=\mathrm{diag}(1/k_T^1,\ldots,1/k_T^N)$. We note that while the normal elastic deformation can be accounted for on the basis of the known geometry at time t_0, the tangential deformation requires consideration of the shear forces both at time t_0 and $t_0+\Delta t$.

Regarding the additional rotational terms implied by the presence of a shear force, the matrix $\bar{\boldsymbol{J}}$ contains the scaled mass moments of inertia:

$$\bar{\boldsymbol{J}}=\frac{1}{\theta\Delta t^2}\boldsymbol{J},\quad \bar{\boldsymbol{m}}_0=\bar{\boldsymbol{J}}\boldsymbol{\omega}_0\Delta t\tag{21}$$

with $\boldsymbol{J}=\mathrm{diag}(J^1,\ldots,J^n)$ being the mass moments of inertia. The vector $\bar{\boldsymbol{m}}_0$, with $\boldsymbol{\omega}_0$ being the rotational velocities, is the rotational equivalent to the effective translational force vector $\bar{\boldsymbol{f}}_0$. In the above, the rotational terms have been discretized in time analogous to the translational terms and the rotational velocities are thus calculated as

$$\boldsymbol{\omega}=\frac{1}{\theta}\left[\frac{\Delta\boldsymbol{\alpha}}{\Delta t}-(1-\theta)\boldsymbol{\omega}_0\right]\tag{22}$$

The matrix $\boldsymbol{R}_0$ concerns the contribution of the total angular momentum balance from the tangential forces and contains entries $\boldsymbol{R}_{iI}=r^i$, $I\in\mathcal{C}^i$ where $\mathcal{C}^i$ is the set of potential contacts associated with particle i.

Finally, the Coulomb criterion is imposed with μ being the inter-particle friction coefficient. For further details on the above formulation (for perfectly rigid particles) we refer to [32].

4.1 Optimality conditions

Following the procedure in "Appendix 3", the KKT conditions associated with (20) can be shown to comprise the

following sets of governing equations pertaining to linear momentum balance:

$$\begin{aligned} &\boldsymbol{t} + \boldsymbol{N}_0\boldsymbol{p} + \hat{\boldsymbol{N}}_0\boldsymbol{q} = \bar{\boldsymbol{f}}_0, \\ &\boldsymbol{t} = \bar{\boldsymbol{M}}\Delta\boldsymbol{x} \end{aligned} \tag{23}$$

angular momentum balance:

$$\begin{aligned} &\boldsymbol{r} - \boldsymbol{R}_0\boldsymbol{q} = \bar{\boldsymbol{m}}_0 \\ &\boldsymbol{r} = \bar{\boldsymbol{J}}\Delta\boldsymbol{\alpha} \end{aligned} \tag{24}$$

sliding friction conditions:

$$\begin{aligned} &|\boldsymbol{q}| - \mu\boldsymbol{p} \leq \boldsymbol{0} \\ &\operatorname{diag}(\boldsymbol{\lambda})(|\boldsymbol{q}| - \mu\boldsymbol{p}) = \boldsymbol{0},\ \boldsymbol{\lambda} \geq \boldsymbol{0}, \end{aligned} \tag{25}$$

and kinematics incorporating elastic deformation characteristics:

$$\begin{aligned} &\boldsymbol{N}_0^{\mathsf{T}}\Delta\boldsymbol{x} + \mu\boldsymbol{\lambda} = \boldsymbol{g}_0 + \boldsymbol{C}_N\boldsymbol{p} \\ &\hat{\boldsymbol{N}}_0^{\mathsf{T}}\Delta\boldsymbol{x} - \boldsymbol{R}_0^{\mathsf{T}}\Delta\boldsymbol{\alpha} = \boldsymbol{C}_T\Delta\boldsymbol{q} + \operatorname{Sgn}(\boldsymbol{q})\boldsymbol{\lambda}. \end{aligned} \tag{26}$$

where Sgn is the signum function. Regarding the kinematics, we note that the variational formulation adopted leads to an apparent dilation proportional to μ. However, as argued in [32] and following [27–29,38–40], this dilation may be viewed as an artifact of the time discretization which, with the exception of a few pathological cases, gradually is reduced as the time step is reduced. Moreover, in [32] it was shown that the dilation, even for rather large time steps, is negligible over a range of common conditions including both instances of highly dynamic and relatively unconfined flows as well as confined quasi-static deformation processes.

4.2 Force based problem

Finally, it is possible to cast (20) in terms of the following force based problem:

$$\begin{aligned} \text{maximize} \quad & -\tfrac{1}{2}\boldsymbol{t}^{\mathsf{T}}\bar{\boldsymbol{M}}^{-1}\boldsymbol{t} - \tfrac{1}{2}\boldsymbol{r}^{\mathsf{T}}\bar{\boldsymbol{J}}^{-1}\boldsymbol{r} \\ & -\boldsymbol{g}_0^{\mathsf{T}}\boldsymbol{p} - \tfrac{1}{2}\boldsymbol{p}^{\mathsf{T}}\boldsymbol{C}_N\boldsymbol{p} - \tfrac{1}{2}\Delta\boldsymbol{q}^{\mathsf{T}}\boldsymbol{C}_T\Delta\boldsymbol{q} \\ \text{subject to} \quad & \boldsymbol{t} + \boldsymbol{N}_0\boldsymbol{p} + \hat{\boldsymbol{N}}_0\boldsymbol{q} = \bar{\boldsymbol{f}}_0 \\ & \boldsymbol{r} - \boldsymbol{R}_0\boldsymbol{q} = \bar{\boldsymbol{m}}_0 \\ & |\boldsymbol{q}| - \mu\boldsymbol{p} \leq \boldsymbol{0} \end{aligned} \tag{27}$$

This is the problem actually solved in numerical calculations. For this purpose, a general second-order cone programming solver, SONIC, recently developed by the authors is employed. This solver is based on much the same principles as the popular codes MOSEK [41] and SeDuMi [42]. Though originally designed with continuum plasticity applications in mind [37], it is ideally suited for the kinds of programs generated by the present granular CD scheme.

4.3 Static limit

Omitting the dynamic forces $\boldsymbol{t}$ and $\boldsymbol{r}$ from the problem (27) gives rise to the following static problem which is valid in the limit of Δt tending to infinity:

$$\begin{aligned} \text{maximize} \quad & -\boldsymbol{g}_0^{\mathsf{T}}\boldsymbol{p} - \tfrac{1}{2}\boldsymbol{p}^{\mathsf{T}}\boldsymbol{C}_N\boldsymbol{p} - \tfrac{1}{2}\Delta\boldsymbol{q}^{\mathsf{T}}\boldsymbol{C}_T\Delta\boldsymbol{q} \\ \text{subject to} \quad & \boldsymbol{N}_0\boldsymbol{p} + \hat{\boldsymbol{N}}_0\boldsymbol{q} = \boldsymbol{f}_{\text{ext}} \\ & \boldsymbol{R}_0\boldsymbol{q} = \boldsymbol{0} \\ & |\boldsymbol{q}| - \mu\boldsymbol{p} \leq \boldsymbol{0} \end{aligned} \tag{28}$$

It is worth noting the similarity of this problem to those that appear from finite element discretizations in continuum plasticity, in particular computational limit analysis [35–37,43]. The above principle is useful for quasi-static problems governed by an internal pseudo-time rather than physical time. Examples include common soil mechanics laboratory tests such as triaxial tests, quasi-static soil-structure interaction problems such as cone penetration, and various applications in the earth sciences where the time scales are such that the deformations are of a quasi-static nature, e.g. [44,45].

The static problem (28) reveals a number of interesting properties related to the indeterminacy of force networks in granular media. It is well known that perfectly rigid particles lead to a situation where the force network solution is non-unique [46–49]. Setting $\boldsymbol{C}_N = \boldsymbol{C}_T = \boldsymbol{0}$ in (28) leads to a linear program where global optimality may be achieved by more than one set of forces. Conversely, for finite values of $\boldsymbol{C}_N$ and $\boldsymbol{C}_T$, the solution is unique, i.e. there is a unique set of contact forces leading to the optimal value of the objective function. This property that elasticity 'regularizes' the problem has an interesting analogy in continuum plasticity where it is well known that the assumption of a rigid-plastic material behaviour leads to a situation where the bearing capacity of a structure comprised of such material can be realized via more than a single statically admissible stress field (the classical example being the Hill and Prandtl solutions for the rigid punch [50]), while the inclusion of elasticity eliminates this non-uniqueness.

5 Numerical examples

In the following, the effects of particle elasticity are studied with reference to the common biaxial test shown in Fig. 5. The initial dimensions of the sample are approximately $16 \times 32\,\text{cm}^2$. Two different initial packings were considered, in the following referred to as loose (porosity of 0.22) and dense (porosity of 0.16). Each sample contains some 8,000 particles that are assumed weightless. The samples were generated by depositing rigid particles under gravity into an open rectangular container with a width of 16 cm. The density of the samples was varied by varying the

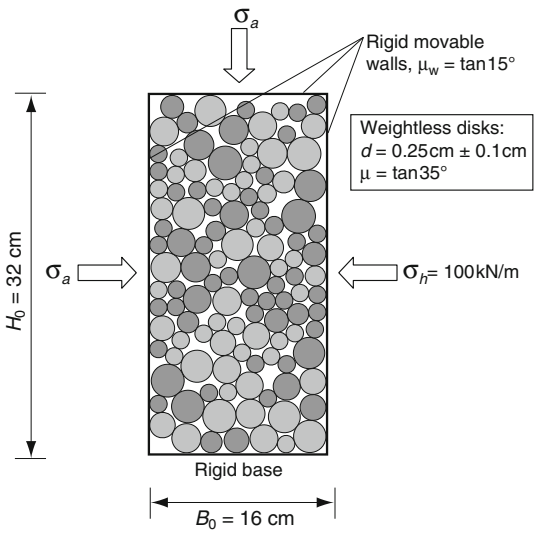

Fig. 5 Setup of biaxial test (actual samples contain approximately 8,000 particles)

inter-particle friction coefficient from a low value to produce the dense sample to higher values to produce the loose sample. Next, constraints specifying vertical and horizontal resultant forces corresponding to a uniform pressure of 100 kN/m were imposed for a number of time steps until the displacement increments between subsequent steps were sufficiently small. This typically required some 8–10 steps. The actual test was then carried out by progressively shifting the upper wall downwards while maintaining constant horizontal reactions. The Lagrange multipliers associated with these latter constraints are the displacements of the walls. These were recorded in each time step, together with the displacement of the upper wall, to eventually infer strains.

5.1 Effects of normal stiffness

We first consider the case where $k_T = \infty$. From a numerical point of view, this case is particularly simple as the term involving $\Delta \boldsymbol{q}$ in (28) vanishes. This in turn means that no information about forces needs to be carried over from one time step to the next. For each packing, three different values of the normal spring constant are used: $k_N = 10, 50$ MN/m, and ∞. In all cases, a total of 400 increments of equal magnitude are used to induce an axial strain of $\varepsilon_a = 0.2$.

The results in terms of plots of deviatoric stress, $\sigma_a - \sigma_h$, versus axial strain, $\varepsilon_a = 1 - H/H_0$, and volumetric strain, $\varepsilon_v = 1 - BH/B_0H_0$, versus axial strain are shown in Fig. 6. The tendency from these figures is—not surprisingly—that the inclusion of particle elasticity has a larger effect on the apparent macroscopic stiffness for the initially dense sample. Indeed, for the dense sample, particle stiffness constitutes the major part of the contribution to the apparent macroscopic

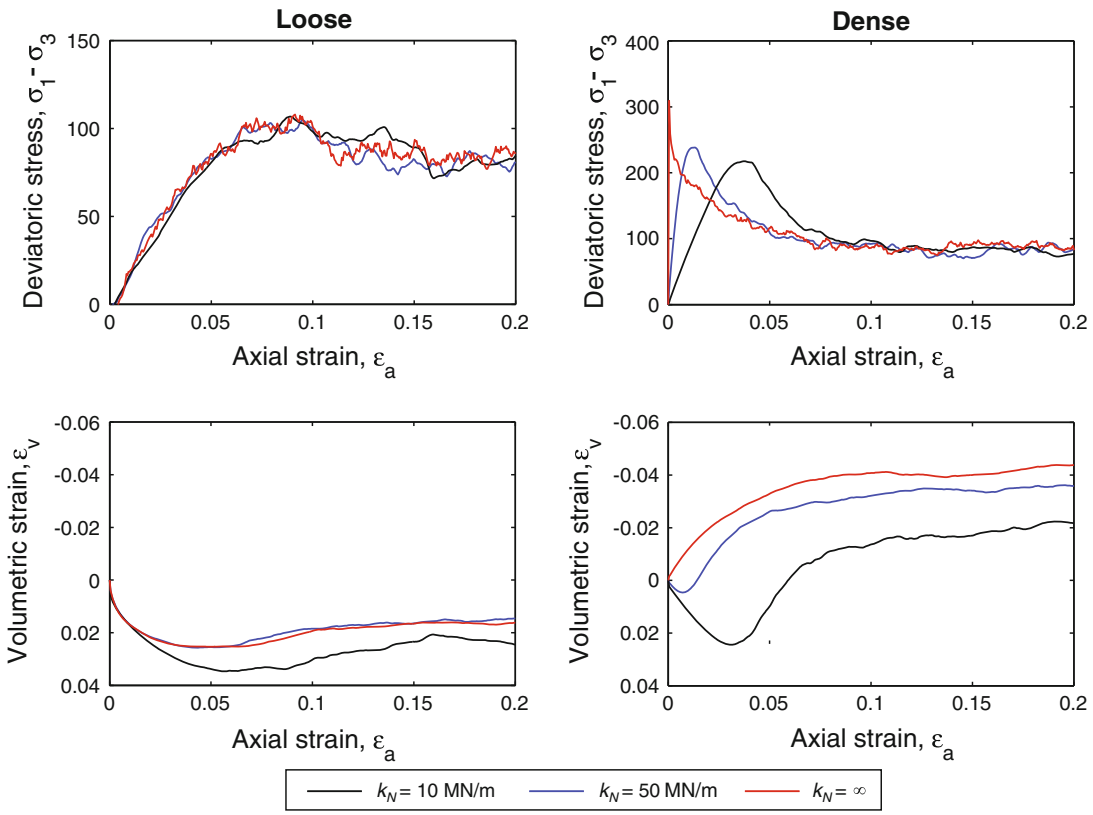

Fig. 6 Biaxial test results for $k_T = \infty$

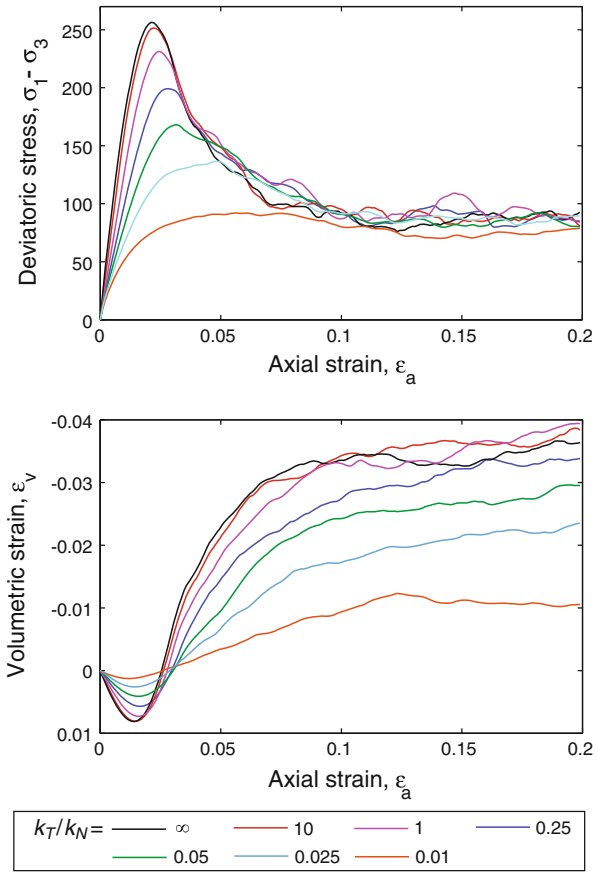

Fig. 7 Biaxial test results for $k_N = 25\,\text{MN/m}$ (dense sample)

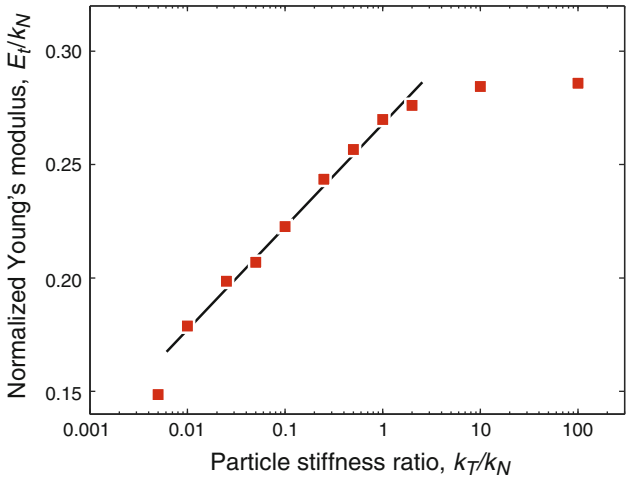

Fig. 8 Dependence of initial tangent Young's modulus on particle stiffness ratio k_T/k_N (dense sample)

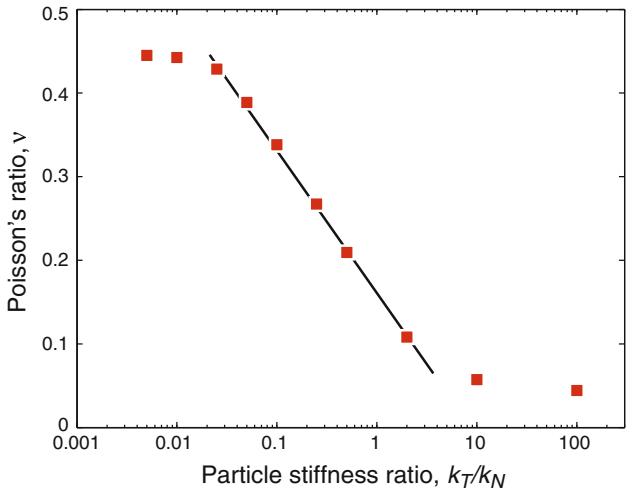

Fig. 9 Dependence of initial tangent Poisson's ratio on particle stiffness ratio k_T/k_N (dense sample)

stiffness. Conversely, for the loose sample, particle rearrangement governs the apparent macroscopic stiffness and particle deformation plays an insignificant role. Regarding strength properties, the results are also in qualitative agreement with what would be expected. That is, the dense sample displays an apparent peak shear stress before tending to the residual level while the loose sample approaches the residual—or critical—state in a monotonically increasing manner. The suppression of the peak by particle compliance is not entirely unexpected either. As the particle stiffness, and thereby the system stiffness, decreases the attainment of the peak stress will be delayed. And when it does occur, particle rearrangements have brought the system into a state that implies a smaller peak stress, if any at all. Finally, we note that, for each of the samples, the macroscopic deviatoric stress reaches a constant value that is independent of the elastic properties while the rate of volumetric strain tends to zero, in agreement with standard continuum plasticity theories.

5.2 Effects of tangent stiffness

Next, we focus on the effects of a finite tangential stiffness. The dense sample is considered with a normal particle stiffness of $k_N = 25\,\text{MN/m}$. The effects of varying the tangential stiffness, k_T, are illustrated in Fig. 7. Again, we observe that an decrease in k_T leads to a more compliant system and thereby a gradual suppression of the peak stress as the stiffness ratio k_T/k_N decreases. The dependence of the system stiffness on the particle stiffness ratio can be characterized by the initial macroscopic tangent Poisson's ratio, ν_t, and tangent Young's modulus, E_t. Assuming plane strain conditions, these are given by

$$\nu_t = \frac{d\varepsilon_a - d\varepsilon_v}{2d\varepsilon_a - d\varepsilon_v} \tag{29}$$

and

$$E_t = \frac{d\sigma_a - d\sigma_h}{2d\varepsilon_a - d\varepsilon_v}(1+\nu_t) \tag{30}$$

The dependence of these parameters on k_T/k_N is shown in Figs. 8 and 9. As expected, the Young's modulus increases with increasing k_T/k_N to ultimately reach an limiting value corresponding to $k_T = \infty$. The Poisson's ratio appears to

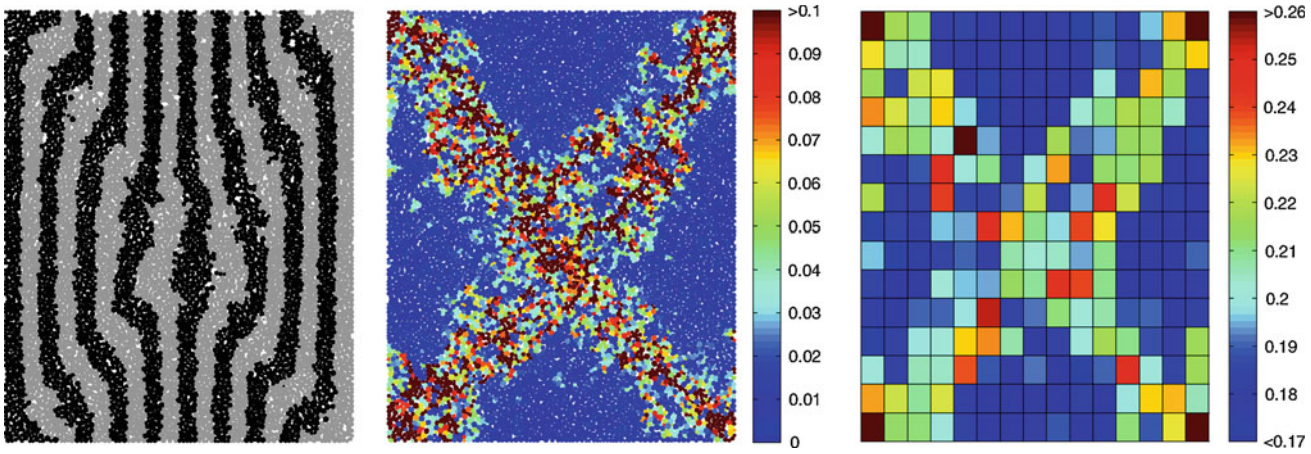

Fig. 10 Biaxial test results for $k_N = k_T = 25$ MNm at $\varepsilon_a = 0.2$ (dense sample): particles colored according to their original position (*left*), particles colored according to relative magnitude of rotation rate (*center*), and distribution of porosity (*right*) (color figure online)

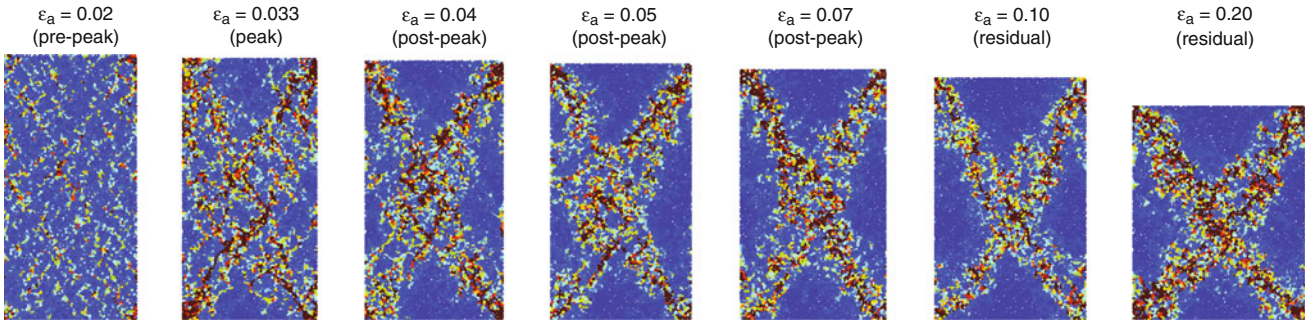

Fig. 11 Evolution of shear bands as gauged by rotation rate for $k_N = k_T = 25$ MN/m (dense sample)

approach 0.5 (corresponding to the incompressible limit) for k_T/k_N tending to zero while, at the other extreme, a value of 0 appears to be asymptotically approached as k_T/k_N tends to infinity. These findings are qualitatively identical to those in [51]. Quantitatively, the present analyses reveals that both E and ν are approximately linear functions of $\log k_T/k_N$ over a large range of realistic particle stiffness ratio, approximately $0.01 \leq k_T/k_N \leq 1$. This provides a convenient means of calibration. For example, to calibrate the particle assembly considered in this example to a typical sand ($0.1 \leq \nu \leq 0.35$), the relevant particle stiffness ratio would be approximately in the range of $0.1 \leq k_T/k_N \leq 1$.

5.3 Shear banding

The load-displacement curves for the dense sample shown in Fig. 6 are quite typical of dense granular media such as sands [52,53]. That is, a characteristic peak in shear stress is observed followed by a decrease until a steady state which is independent of the initial density. In terms of deformations, the behaviour is characterized by an initial compaction followed by a dilation that reaches its maximum extent around the peak stress, after which the rate of volumetric straining eventually tends to zero as the steady, or critical, state is approached. This behaviour is again observed in Fig. 7 although the peak, as already discussed, is suppressed by decreasing the k_T/k_N ratio.

In physical experiments, it is often observed that the peak shear stress is accompanied by the formation of one or more bands of localized deformation. These shear bands may form quite abruptly [52] or gradually become more pronounced as the deformation proceeds [53]. Figures 10 and 11, which are concerned with the dense sample and a particle stiffness ratio, $k_T/k_N = 1$, illustrate the latter type of behaviour. Firstly, in Fig. 10, the state of deformation at an axial strain of $\varepsilon_a = 0.2$ is shown together with the rate of rolling and the local porosities in the sample. We here observe a good correlation between the zones of intense deformation and rate of particle rolling. Moreover, the local porosities are also rather indicative of the location of these zones, with the porosity increasing quite substantially inside the shear bands. Assuming a correlation between density and shear strength, it is not difficult to appreciate that the decrease in shear strength after the peak and the increase in porosity inside the shear bands are consequences of each other.

Finally, in Fig. 11, the rate of rolling is shown at difference stages of the loading. From a relatively homogeneous distribution prior to the peak, the zones of particle rolling gradually localize after the peak to eventually define two quite distinct bands at the critical state.

6 Conclusions

A granular CD formulation for elastically deformable particles has been detailed. The resulting scheme bears some similarity to traditional MD schemes in that the consideration of a finite contact stiffness implies the possibility for an elastically reversible inter-particle penetration. We show that the inclusion of particle elasticity reproduces the more basic case of rigid particles in the limit of the inter-particle stiffness tending to infinity. Moreover, in contrast to MD, there are no algorithmic repercussions from operating with a large or, in the extreme case infinite, stiffness. Indeed, the same algorithm is used regardless of the contact stiffness, with perfect rigidity being a limiting case that allows for certain simplifications. In the present paper we have only considered the case of linear elasticity but extension to nonlinear elasticity is entirely possible as is the consideration of more complex contact models incorporating hardening, viscous effects, etc.

Appendix 1: Three-dimensional formulation

The two-dimensional formulation discussed in the main part of the paper may be extended to three dimensions in a number of ways. In the following, one possibility is outlined.

Compared to the two-dimensional case, the main complication is that the direction of the shear force is unknown a priori, the only requirement being that it is orthogonal to the normal contact direction. The basic idea of the following three-dimensional formulation, sketched in Fig. 12, is to consider a normal force directed along the particle normal as in the two-dimensional case. The shear forces are accounted for by separate force vector $\boldsymbol{q}^I = (q_x^I, q_y^I, q_z^I)$ which must satisfy

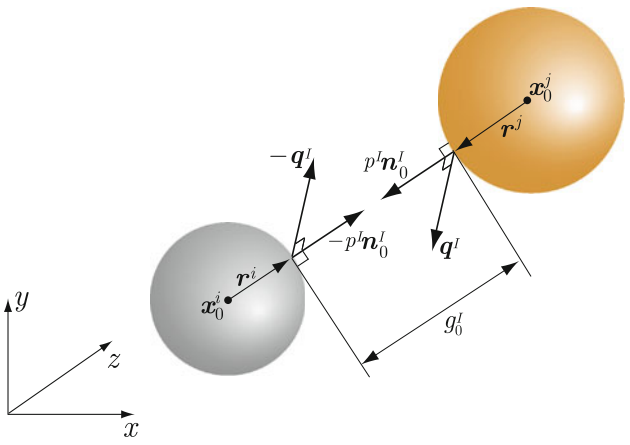

Fig. 12 Frictional contact geometry in three dimensions

$$\left(\boldsymbol{n}_0^I\right)^{\mathsf{T}} \boldsymbol{q}^I = 0 \tag{31}$$

This condition is imposed explicitly in the final optimization problem.

With the above definition of forces, linear momentum balance is given by

$$\begin{aligned} \bar{m}^i \Delta \boldsymbol{x}^i + p^I \boldsymbol{n}_0^I + \boldsymbol{q}^I &= \bar{\boldsymbol{f}}_0^i \\ \bar{m}^j \Delta \boldsymbol{x}^j - p^I \boldsymbol{n}_0^I - \boldsymbol{q}^I &= \bar{\boldsymbol{f}}_0^j \end{aligned} \tag{32}$$

while the angular momentum balance equations read:

$$\begin{aligned} \bar{J}^i \Delta \boldsymbol{\alpha}^i - \boldsymbol{r}_0^i \times \boldsymbol{q}^I &= \bar{\boldsymbol{m}}_0^i \\ \bar{J}^j \Delta \boldsymbol{\alpha}^j + \boldsymbol{r}_0^j \times \boldsymbol{q}^I &= \bar{\boldsymbol{m}}_0^j \end{aligned} \tag{33}$$

Similarly to the two-dimensional case, the frictional sliding condition is given by

$$||\boldsymbol{q}^I|| - \mu p^I \leq 0 \tag{34}$$

Furthermore, for each contact, the quadratic term in the objective function of (20), now reads

$$\tfrac{1}{2} C_N (p^I)^2 + \tfrac{1}{2} C_T (\Delta \boldsymbol{q}^I)^{\mathsf{T}} \Delta \boldsymbol{q}^I \tag{35}$$

where $\Delta \boldsymbol{q} = \boldsymbol{q} - \boldsymbol{q}_0$, with $\boldsymbol{q}_0$ being the known shear force at the beginning of the time step as in the two-dimensional case. In summary, the three-dimensional formulation follows the two-dimensional formulation closely, the only essential modification being that the direction of the shear force is unknown a priori, necessitating the orthogonality condition (31). Finally, the optimization problems generated by the above three-dimensional formulation can be solved using the same second-order cone programming algorithm as in the two-dimensional case.

Appendix 2: KKT optimality conditions

We consider the saddle-point problem representing the frictionless contact problem:

$$\begin{aligned} \min_{\Delta \boldsymbol{x}} \max_{\boldsymbol{p}} \quad & \left\{ \tfrac{1}{2} \Delta \boldsymbol{x}^{\mathsf{T}} \bar{\boldsymbol{M}} \Delta \boldsymbol{x} - \Delta \boldsymbol{x}^{\mathsf{T}} \bar{\boldsymbol{f}}_0 \right\} \\ & + \left\{ \Delta \boldsymbol{x}^{\mathsf{T}} \boldsymbol{N}_0 \boldsymbol{p} - \boldsymbol{g}_0^{\mathsf{T}} \boldsymbol{p} \right\} \\ \text{subject to} \quad & \boldsymbol{p} \geq \boldsymbol{0} \end{aligned} \tag{36}$$

The first-order KKT optimality conditions associated with this problem can be derived using the following procedure [35,54–56]. The inequality constraints are first converted into equality constraints by subtraction of positively restricted slack variables $\boldsymbol{s}$. The objective function is then augmented by a logarithmic barrier function which eliminates the need to

make explicit reference to the fact that $\boldsymbol{s} \geq \boldsymbol{0}$. The modified, equality constrained, problem is given by

$$\begin{aligned} \min_{\Delta \boldsymbol{x}} \max_{\boldsymbol{p},\boldsymbol{s}} \quad & \left\{\tfrac{1}{2}\Delta \boldsymbol{x}^{\mathsf{T}} \bar{\boldsymbol{M}} \Delta \boldsymbol{x} - \Delta \boldsymbol{x}^{\mathsf{T}} \bar{\boldsymbol{f}}_0\right\} \\ & + \left\{\Delta \boldsymbol{x}^{\mathsf{T}} \boldsymbol{N}_0 \boldsymbol{p} - \boldsymbol{g}_0^{\mathsf{T}} \boldsymbol{p}\right\} + \beta \textstyle\sum_{I \in \mathcal{C}} \ln s^I \\ \text{subject to} \quad & \boldsymbol{p} - \boldsymbol{s} = \boldsymbol{0} \end{aligned} \tag{37}$$

where $\beta > 0$ is an arbitrarily small constant and $\mathcal{C}$ is the set of potential contacts. The standard Lagrange multiplier technique then applies, i.e. the solution to (37) is found by requiring stationarity of the Lagrangian

$$\begin{aligned} L = {} & \tfrac{1}{2}\Delta \boldsymbol{x}^{\mathsf{T}} \bar{\boldsymbol{M}} \Delta \boldsymbol{x} + \Delta \boldsymbol{x}^{\mathsf{T}} (\boldsymbol{N}_0 \boldsymbol{p} - \bar{\boldsymbol{f}}_0) - \boldsymbol{g}_0^{\mathsf{T}} \boldsymbol{p} \\ & + \beta \textstyle\sum_{I \in \mathcal{C}} \ln s^I + \boldsymbol{\lambda}^{\mathsf{T}} (\boldsymbol{p} - \boldsymbol{s}) \end{aligned} \tag{38}$$

where $\boldsymbol{\lambda}$ are Lagrange multipliers. The stationary conditions are given by

$$\begin{aligned} \frac{\partial L}{\partial \boldsymbol{x}} &= \bar{\boldsymbol{M}} \Delta \boldsymbol{x} - \bar{\boldsymbol{f}}_0 + \boldsymbol{N}_0 \boldsymbol{p} = 0 \\ \frac{\partial L}{\partial \boldsymbol{p}} &= \boldsymbol{N}_0^{\mathsf{T}} \Delta \boldsymbol{x} - \boldsymbol{g}_0 + \boldsymbol{\lambda} = \boldsymbol{0} \\ \frac{\partial L}{\partial \boldsymbol{\lambda}} &= \boldsymbol{p} - \boldsymbol{s} = \boldsymbol{0} \\ \frac{\partial L}{\partial s^I} &= \frac{\beta}{s^I} - \lambda^I = 0 \implies s^I \lambda^I = \beta, \quad I \in \mathcal{C} \end{aligned} \tag{39}$$

By letting β tend to zero while bearing in mind that $\boldsymbol{s} \geq 0$, the KKT conditions (11) are recovered.

Appendix 3: Alternative variational principles for frictionless elastic particles

The governing equations (17) may be cast in a number of different ways besides (18) and (19). The perhaps most direct way is to include a quadratic term in the contact forces into (12). We thus have

$$\begin{aligned} \min_{\Delta \boldsymbol{x}} \max_{\boldsymbol{p}} \quad & \left\{\tfrac{1}{2}\Delta \boldsymbol{x}^{\mathsf{T}} \bar{\boldsymbol{M}} \Delta \boldsymbol{x} - \Delta \boldsymbol{x}^{\mathsf{T}} \bar{\boldsymbol{f}}_0\right\} \\ & + \left\{\Delta \boldsymbol{x}^{\mathsf{T}} \boldsymbol{N}_0 \boldsymbol{p} - \boldsymbol{g}_0^{\mathsf{T}} \boldsymbol{p} - \tfrac{1}{2}\boldsymbol{p}^{\mathsf{T}} \boldsymbol{C} \boldsymbol{p}\right\} \\ \text{subject to} \quad & \boldsymbol{p} \geq \boldsymbol{0} \end{aligned} \tag{40}$$

While this problem reproduces the governing equations (17) directly, solving for the min part first does not produce a pure force based problem. Similarly, solving first with respect to the max part does not result in a pure displacement based problem.

To arrive at a pure displacement based problem, (12) is instead extended by introducing a new set of variables, $\boldsymbol{e}$, such that we have

$$\begin{aligned} \min_{\Delta \boldsymbol{x}, \boldsymbol{e}} \max_{\boldsymbol{p}} \quad & \tfrac{1}{2}\Delta \boldsymbol{x}^{\mathsf{T}} \bar{\boldsymbol{M}} \Delta \boldsymbol{x} + \tfrac{1}{2}\boldsymbol{e}^{\mathsf{T}} \boldsymbol{D} \boldsymbol{e} - \Delta \boldsymbol{x}^{\mathsf{T}} \bar{\boldsymbol{f}}_0 \\ & + \boldsymbol{p}^{\mathsf{T}} \left(\boldsymbol{N}_0^{\mathsf{T}} \Delta \boldsymbol{x} - \boldsymbol{g}_0 - \boldsymbol{e}\right) \\ \text{subject to} \quad & \boldsymbol{p} \geq \boldsymbol{0} \end{aligned} \tag{41}$$

where $\boldsymbol{D} = \boldsymbol{C}^{-1}$. The new variables $\boldsymbol{e}$ here represent the total elastic normal deformation (see Fig. 3). We note the similarity of this problem to the Hu–Washizu variational principle [34]. Finally, a problem containing only kinematic variables as unknowns follows by solving the max part of the above problem:

$$\begin{aligned} \text{minimize} \quad & \tfrac{1}{2}\Delta \boldsymbol{x}^{\mathsf{T}} \bar{\boldsymbol{M}} \Delta \boldsymbol{x} + \tfrac{1}{2}\boldsymbol{e}^{\mathsf{T}} \boldsymbol{D} \boldsymbol{e} - \Delta \boldsymbol{x}^{\mathsf{T}} \bar{\boldsymbol{f}}_0 \\ \text{subject to} \quad & \boldsymbol{N}_0^{\mathsf{T}} \Delta \boldsymbol{x} \leq \boldsymbol{g}_0 + \boldsymbol{e} \end{aligned} \tag{42}$$

We note that the objective function is here the time discrete action integral associated with a collection of linear elastically deformable particles. The KKT conditions are given by

$$\begin{aligned} & \bar{\boldsymbol{M}} \Delta \boldsymbol{x} + \boldsymbol{N}_0 \boldsymbol{p} = \bar{\boldsymbol{f}}_0 \\ & \boldsymbol{N}_0^{\mathsf{T}} \Delta \boldsymbol{x} \leq \boldsymbol{g}_0 + \boldsymbol{e} \\ & \boldsymbol{p} = \boldsymbol{D} \boldsymbol{e} \\ & \boldsymbol{p} \geq \boldsymbol{0} \\ & \boldsymbol{P}(\boldsymbol{N}_0^{\mathsf{T}} \Delta \boldsymbol{x} - \boldsymbol{g}_0 - \boldsymbol{e}) = \boldsymbol{0} \end{aligned} \tag{43}$$

which are equivalent to those of (17).

References

1. Cundall, P.A., Strack, O.D.L.: A discrete numerical model for granular assemblies. Geotechnique **29**, 47–65 (1979)
2. Cundall, P.A., Hart, D.H.: Numerical modelling of discontinua. Eng. Comput. **9**, 101–113 (1992)
3. Belheine, N., Plassiard, J.P., Donze, F.V., Darve, F., Seridi, A.: Numerical simulation of drained triaxial test using 3d discrete element modeling. Comput. Geotech. **36**, 320–331 (2009)
4. Ng, T.T.: Input parameters of discrete element methods. J. Eng. Mech. **132**, 723–729 (2006)
5. Antony, S.J., Kruyt, N.P.: Role of interparticle friction and particle-scale elasticity in the shear-strength mechanism of three-dimensional granular media. Phys. Rev. E **79**, 031308 (2009)
6. Ding, Y., Gravish, N., Goldman, D.I.: Drag induced lift in granular media. Phys. Rev. Lett. **106**, 028001 (2011)
7. Moreau, J.J.: Bounded variation in time. In: Panagiotopoulos, P.D., Strang, G. (eds.) Topics in Nonsmooth Mechanics, vol. 1, pp. 1–74 (1987)
8. Moreau, J.J.: Unilateral contact and dry friction in finite freedom dynamics. In: Moreau, J.J., Panagiotopoulos, P. (eds.) Non-Smooth Mechanics and Applications, CISM Courses and Lectures, vol. 302, pp. 1–82. Springer, Berlin (1988)

9. Moreau, J.J.: Some numerical methods in multibody dynamics: application to granular materials. Eur. J. Mech. A Solids **13**, 93–114 (1994)
10. Jean, M.: The non-smooth contact dynamics method. Comput. Methods Appl. Mech. Eng. **177**, 235–257 (1999)
11. Radjai, F., Michel, J., Moreau, J.J., Roux, S.: Force distributions in dense two-dimensional granular systems. Phys. Rev. Lett. **77**, 274–277 (1996)
12. Nouguier-Lehon, C., Cambou, B., Vincens, E.: Influence of particle shape and angularity on the behavior of granular materials: a numerical analysis. Int. J. Numer. Anal. Methods Geomech. **27**, 1207–1226 (2003)
13. McNamara, S., Herrmann, H.: Measurement of indeterminacy in packings of perfectly rigid disks. Phys. Rev. E **70**, 061303 (2004)
14. Renouf, M., Dubois, F., Alart, P.: A parallel version of the non smooth contact dynamics algorithm applied to the simulation of granular media. J. Comput. Appl. Math. **168**, 375–382 (2004)
15. Taboada, A., Chang, K.J., Radjai, F., Bouchette, F.: Rheology force transmission and shear instabilities in frictional granular media from biaxial numerical test using the contact dynamics method. J. Geophys. Res. **110**, 1–24 (2005)
16. Staron, L., Hinch, E.J.: Study of the collapse of granular columns using two-dimensional discrete-grain simulation. J. Fluid Mech. **545**, 1–27 (2005)
17. Bartels, G., Unger, T., Kadau, D., Wolf, D.E., Kertesz, J.: The effect of contact torques on porosity of cohesive powders. Granul. Matter **7**, 139–143 (2005)
18. Kadau, D., Schwesig, D., Theuerkauf, J., Wolf, D.E.: Influence of particle elasticity in shear testers. Granul. Matter **8**, 35–40 (2006)
19. Saussine, G., Cholet, C., Gautier, P.E., Dubois, F., Bohatier, C., Moreau, J.J.: Modelling ballast behaviour under dynamic loading part 1.: A 2D polygonal discrete element method approach. Comput. Methods Appl. Mech. Eng. **195**, 2841–2859 (2006)
20. Staron, L., Hinch, E.J.: The spreading of a granular mass: role of grain properties and initial conditions. Granul. Matter **9**, 205–217 (2007)
21. Ries, A., Wolf, D.E., Unger, T.: Shear zones in granular media: three-dimensional contact dynamics simulation. Phys. Rev. E **76**, 051301 (2007)
22. Radjai, F., Richefeu, V.: Contact dynamics as a nonsmooth discrete element method. Mech. Mater. **41**, 715–728 (2009)
23. Stegmann, T., Török, J., Brendel, L., Wolf, D.E.: Minimal dissipation theory and shear bands in biaxial tests. Granul. Matter **13**, 565–572 (2011)
24. Estrada, N., Azema, E., Radjai, F., Taboada, A.: Identification of rolling resistance as a shape parameter in sheared granular media. Phys. Rev. E **84**, 011306 (2011)
25. Kadau, D., Andrade, J.S. Jr., Herrman, H.J.: A micromechanical model of collapsing quicksand. Granul. Matter **13**, 219–223 (2011)
26. Lagree, P.Y., Staron, L., Popinet, S.: The granular column collapse as a continuum: validity of a two-dimensional Navier–Stokes model with a $\mu(i)$-rheology. J. Fluid Mech. **686**, 378–408 (2011)
27. Petraa, C., Gavreab, B., Anitescu, M., Potraa, F.: A computational study of the use of an optimization-based method for simulating large multibody systems. Optim. Methods Softw. **24**, 871–894 (2009)
28. Tasora, A., Anitescu, M.: A convex complementarity approach for simulating large granular flows. J. Comput. Nonlinear Dyn. **5**, 031004 (2010)
29. Tasora, A., Anitescu, M.: A matrix-free cone complementarity approach for solving large-scale, nonsmooth, rigid body dynamics. Comput. Methods Appl. Mech. Eng. **200**, 439–453 (2011)
30. Acary, V., Brogliato, B.: Numerical Methods for Nonsmooth Dynamical Systems. Springer, Berlin (2008)
31. Cambou, B., Jean, M., Radjai, F.: Micromechanics of Granular Materials. Wiley, London (2009)
32. Krabbenhoft, K., Lyamin, A.V., Huang, J., Vicente da Silva M.: Granular contact dynamics using mathematical programming methods. Comput. Geotech. **43**, 165–176 (2012, in press)
33. Wood, W.L.: Practical Time-Stepping Schemes. Oxford University Press, Oxford (1990)
34. Washizu, K.: Variational Methods of Elasticity and Plasticity. Pergamon Press, Oxford (1982)
35. Krabbenhoft, K., Lyamin, A.V., Sloan, S.W., Wriggers, P.: An interior-point method for elastoplasticity. Int. J. Numer. Methods Eng. **69**, 592–626 (2007)
36. Krabbenhoft, K., Lyamin, A.V., Sloan, S.W.: Formulation and solution of some plasticity problems as conic programs. Int. J. Solids Struct. **44**, 1533–1549 (2007)
37. Krabbenhoft, K., Lyamin, A.V.: Computational Cam clay plasticity using second-order cone programming. Comput. Methods Appl. Mech. Eng. **209–212**, 239–249 (2012)
38. Anitescu, M., Hart, G.D.: A constraint-stabilized time-stepping approach for rigid multibody dynamics with joints, contact and friction. Int. J. Numer. Methods Eng. **60**, 2335–2371 (2004)
39. Anitescu, M.: Optimization-based simulation of nonsmooth rigid multibody dynamics. Math. Program. A **105**, 113–143 (2006)
40. Tasora, A., Anitescu, M.: An iterative approach for cone complementarity problems for nonsmooth dynamics. Comput. Optim. Appl. **47**, 207–235 (2010)
41. Andersen, E.D., Roos, C., Terlaky, T.: On implementing a primal-dual interior-point method for conic quadratic optimization. Math. Program. **95**, 249–277 (2003)
42. Sturm, J.F.: SeDuMi 1.02, a MATLAB toolbox for optimizing over symmetric cones. Optim. Methods Softw. **11–12**, 625–653 (1999) http://sedumi.mcmaster.ca/
43. Krabbenhoft, K., Lyamin, A.V., Hjiaj, M., Sloan, S.W.: A new discontinuous upper bound limit analysis formulation. Int. J. Numer. Methods Eng. **63**, 1069–1088 (2005)
44. Souloumiac, P., Leroy, Y.M., Maillot, B., Krabbenhoft, K.: Predicting stress distributions in fold-and-thrust belts and accretionary wedges by optimization. J. Geophys. Res. **114**, B09404 (2009)
45. Souloumiac, P., Krabbenhoft, K., Leroy, Y.M., Maillot, B.: Failure in accretionary wedges with the maximum strength theorem: numerical algorithm and 2d validation. Comput. Geosci. **14**, 793–811 (2010)
46. Radjai, F., Brendel, L., Roux, S.: Nonsmoothness, indeterminacy, and friction in two-dimensional arrays of rigid particles. Phys. Rev. E **861**, 54 (1996)
47. Snoeijer, J.H., Vlugt, T.J.H., van Hecke, M., van Saarloos, W.: Force network ensemble: a new approach to static granular matter. Phys. Rev. Lett. **054302**, 92 (2004)
48. McNamara, S., Garcia-Rojo, R., Herrmann, H.: Indeterminacy and the onset of motion in a simple granular packing. Phys. Rev. E **021304**, 72 (2005)
49. Unger, T., Kertesz, J., Wolf, D.E.: Force indeterminacy in the jammed state of hard disks. Phys. Rev. Lett. **178001**, 94 (2005)
50. Chen, W.F., Han, D.J.: Plasticity for Structural Engineers. Springer, New York (1988)
51. Mohamed, A., Gutierrez, M.: Comprehensive study of the effects of rolling resistance on the stressstrain and strain localization behavior of granular materials. Granul. Matter **12**, 527–541 (2010)
52. Lade, P.V., Wang, Q.: Analysis of shear banding in true triaxial tests on sand. J. Eng. Mech. **127**, 762–768 (2001)
53. Rechenmacher, A.L.: Grain-scale processes governing shear band initiation and evolution in sands. J. Mech. Phys. Solids **54**, 22–45 (2006)

54. Nash, S.G., Sofer, A.: Linear and Nonlinear Programming. McGraw-Hill, New York (1996)
55. Vanderbei, R.J.: Linear Programming: Foundations and Extensions. Springer, Berlin (2001)
56. Boyd, S., Vandenberghe, L.: Convex Optimization. Cambridge University Press, Cambridge (2006)